nature energy

Article

https://doi.org/10.1038/s41560-024-01616-5

Tailoring planar strain for robust structural stability in high-entropy layered sodium oxide cathode materials

Received: 31 January 2024

Accepted: 24 July 2024

Published online: 26 August 2024

Check for updates

Feixiang Ding[1,2], Pengxiang Ji[1,3], Zhen Han[1], Xueyan Hou[1], Yang Yang[1,3], Zilin Hu[1,3], Yaoshen Niu[1], Yuan Liu[1,3], Jiao Zhang[1], Xiaohui Rong[1,3,4], Yaxiang Lu[1,2,3,4] ✉, Huican Mao[5] ✉, Dong Su[1,2,3] ✉, Liquan Chen[1,2,3,4] & Yong-Sheng Hu[1,2,3,4] ✉

High-entropy oxides have expanded the potential for high-performance Na-ion battery cathodes due to their vast compositional space and entropy-driven stabilization. However, a rational design approach for optimizing their composition is still lacking. Here, we develop an O3-type oxide cathode composed of all-3*d* transition metals, $NaNi_{0.3}Cu_{0.1}Fe_{0.2}Mn_{0.3}Ti_{0.1}O_2$ (NCFMT), which exhibits improved reversible specific capacity and exceptional cycling stability. Replacing Ti^{4+} with Sn^{4+} ions ($NaNi_{0.3}Cu_{0.1}Fe_{0.2}Mn_{0.3}Sn_{0.1}O_2$; NCFMS) results in poor structural reversibility and diminished cycling stability. Our investigations suggest that the structural integrity of the layered cathode is affected by the compatibility of constituent elements within the transition metal layers (TMO_2). In NCFMS, planar strain induced by metal-ion displacement triggers elemental segregation and crack formation during repeated cycling. In contrast, NCFMT demonstrates a robust structural framework for stable Na^+ storage due to its high mechanochemical compatibility among constituent elements. This understanding provides insights for designing outstanding layered high-entropy cathode materials.

Na-ion batteries (NIBs) are an attractive technology for stationary energy storage because of their low production cost and material abundance[1]. The success of NIBs relies heavily on the development of remarkable cathode compounds. Among various candidates, layered transition metal (TM) oxide cathodes (Na_xTMO_2) have attracted extensive interest from both academic and industrial sectors[2–5] because of their high theoretical specific capacity and advantages in large-scale manufacturing. However, most layered oxide materials face challenges such as severe structural degradation or low practical reversible specific capacity during cycling. Addressing these issues is crucial for the widespread application of NIBs.

During cycling in O3-type Na_xTMO_2, the extraction of Na^+ increases O–O electrostatic repulsion, causing expansion and subsequent contraction of the *c* spacing. This triggers a structural transformation from O3 to P3 and eventually to OP2(O1)[6]. At the same time, the oxidation of active TM ions contracts TMO_6 octahedron structure units, decreasing the lattice parameter *a*/*b* (ref. 7). The accumulation of local displacement of anionic and cationic species, along with changes in TM–O bond

[1]Key Laboratory for Renewable Energy, Beijing Key Laboratory for New Energy Materials and Devices, Beijing National Laboratory for Condensed Matter Physics, Institute of Physics, Chinese Academy of Sciences, Beijing, China. [2]Huairou Division, Institute of Physics, Chinese Academy of Sciences, Beijing, China. [3]College of Materials Science and Optoelectronic Technology, University of Chinese Academy of Sciences, Beijing, China. [4]Yangtze River Delta Physics Research Center Co. Ltd, Liyang, China. [5]Department of Energy Storage Science and Engineering, School of Metallurgical and Ecological Engineering, University of Science and Technology Beijing, Beijing, China. ✉e-mail: yxlu@iphy.ac.cn; hcmao@ustb.edu.cn; dongsu@iphy.ac.cn; yshu@iphy.ac.cn

https://doi.org/10.1038/s41560-024-01616-5

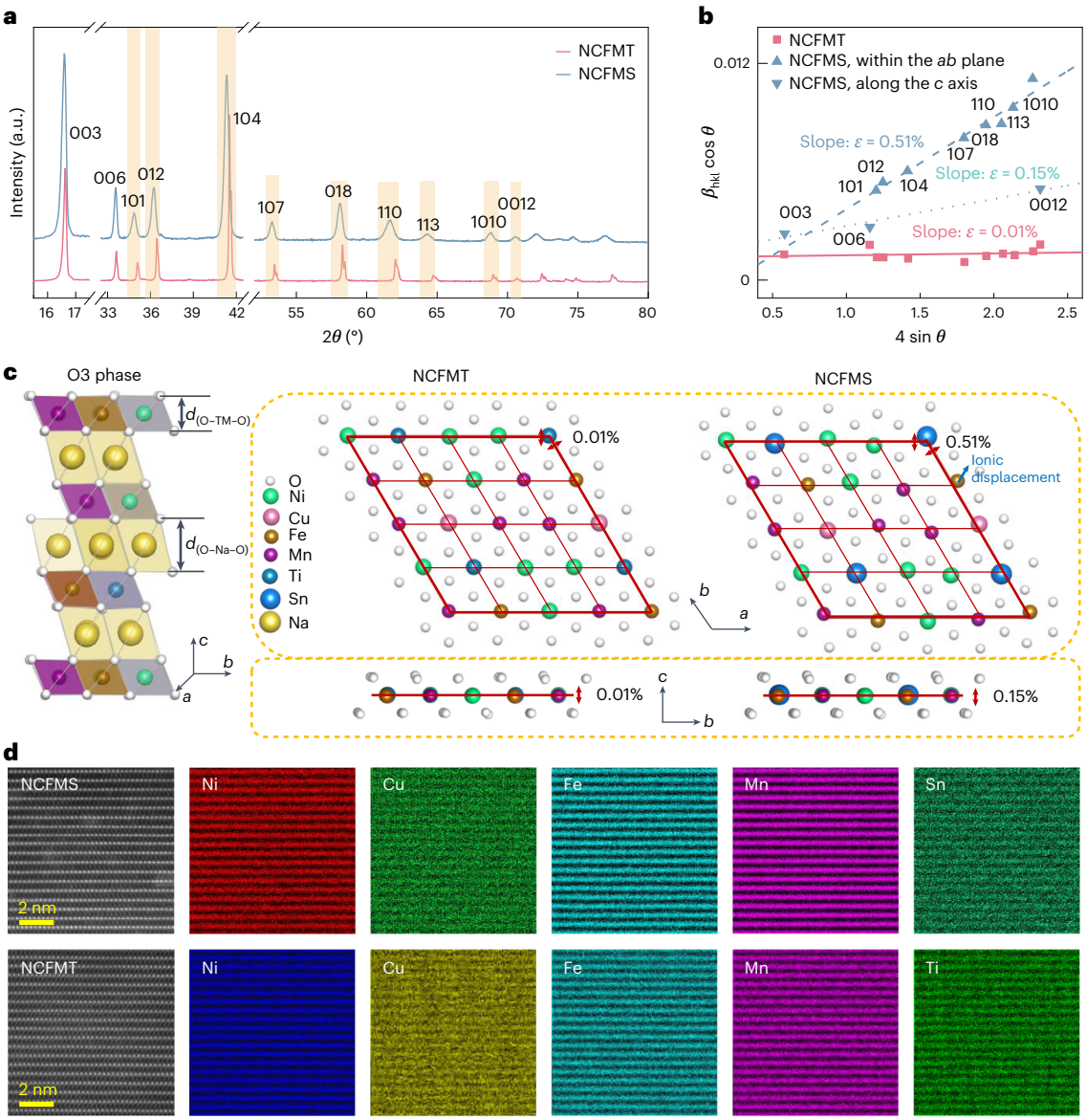

Fig. 1 | Atomic structure difference between NCFMT and NCFMS. a, XRD patterns of NCFMT and NCFMS. a.u., arbitrary units. **b**, ε calculated using Williamson–Hall analysis. The anisotropic strain distribution in the NCFMS material was evaluated by using independent fits to *hkl* reflections relative to reflections primarily within the *ab* plane (dashed line) or between the *ab* planes (dotted line). **c**, Structural model of O3 phase and schematic showing the correlation between strain distribution and ionic displacement for NCFMT and NCFMS viewed perpendicular and parallel to the TMO_2 layers. **d**, Atomic EDS mapping of element distributions in the NCFMS and NCFMT, including the corresponding HAADF-STEM image of the lattice structure along the [110] zone axes.

lengths, raise stress levels and induce planar gliding or chemical bond breaking. These processes result in microcracks, oxygen loss and cation migration[8–12]. To enhance the durability of Na-ion layered cathodes, it is crucial to construct robust and flexible TM oxide slabs (TMO_2), which serve as a structural framework facilitating both Na^+-migration and electron-diffusion pathways.

High-entropy oxide cathode materials[13–16], consisting of five to nine metal ions at the TM site in a solid-solution phase, offer excellent electrochemical performances with high energy density, rate capability and capacity retention. Moreover, their improved thermal stability addresses long-standing safety concerns in battery technology[13,17,18]. The superior properties stem from high configurational entropy, local disorder and a synergy effect among individual elements, which contribute to the structural stabilization during Na^+ (de)intercalation. Despite these advantages, research on high-entropy oxide materials is still in its infancy, and no design rules have been systematically established for creating optimal compositions suitable for commercial success. In particular, when reducing configurational entropy from an ultrahigh to a moderate value to balance entropy increase and capacity utilization, severe lattice distortion or strain may occur due to the prominent mismatches in ionic mass, size and bond state[19–23]. Recent studies reveal that lattice distortion in high-entropy systems affects physicochemical characteristics, yielding distinct properties[19–21]. For example, distorted lattices scatter heat-carrying phonons, lowering the lattice thermal conductivity of n-type PbSe-based high-entropy material[19]. Additionally, lattice distortion strengthens electron scattering and reduces the conductivity of $Bi_4Ti_3O_{12}$-based medium-entropy films[21]. However, the influence of lattice distortion on the structural integrity of a layered cathode with reversible cationic redox remains unexplored. Therefore, developing a design strategy to effectively tailor lattice distortion while maximizing entropy-dominated phase stabilization is crucial for promoting the development of outstanding layered high-entropy cathode materials.

https://doi.org/10.1038/s41560-024-01616-5

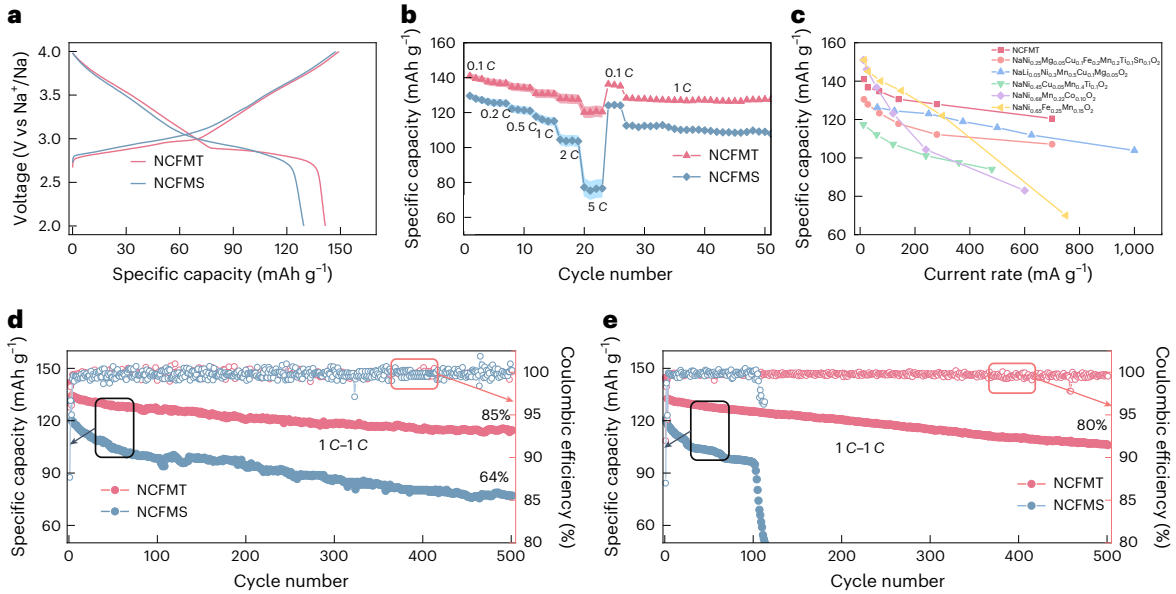

Fig. 2 | Superior electrochemical performance of NCFMT over NCFMS. **a**, The charge–discharge profiles at 0.1 *C* (here 1 *C* is defined as 140 mA g^{-1}) during the first cycle in half cells. **b**, Rate capability at rates ranging from 0.1 *C* to 5 *C*. The shading shows the s.d. calculated from at least three cells. **c**, Comparison of the rate capabilities of the NCFMT cathode with previously reported O3-type cathodes for NIBs performed in the same voltage range. **d**, The cycling performance at room temperature. **e**, High-temperature cycling performance at 45 °C.

In this work, we compare two O3-type layered high-entropy oxides: $NaNi_{0.3}Cu_{0.1}Fe_{0.2}Mn_{0.3}Ti_{0.1}O_2$ (NCFMT), with only 3*d* TMs in TMO_2 slabs, and $NaNi_{0.3}Cu_{0.1}Fe_{0.2}Mn_{0.3}Sn_{0.1}O_2$ (NCFMS), which replaces Ti with Sn in TMO_2 slabs. Both materials exhibit uniform element distributions in their pristine states, but NCFMS exhibits planar strain due to lattice distortion caused by mismatches of ionic size, mass and valence-electron configuration. The inherited strain in TMO_2 slabs and accumulated lattice strain during repeated TM redox facilitate thermodynamically favourable metal-ion migration. This leads to elemental segregation and crack formation (metal-ion dissolution) in the interior and surface of NCFMS cathode particles, respectively, as confirmed by combined aberration-corrected high-angle annular dark-field scanning transmission electron microscopy (HAADF-STEM) with energy-dispersive X-ray spectroscopy (EDS) analysis. By contrast, NCFMT, with better mechanochemical compatibility among 3*d* TMs, does not exhibit the degradation mechanisms observed in NCFMS, resulting in improved cycling stability in both half-cell and full-cell batteries. This work highlights the importance of elemental selection for designing high-performance layered high-entropy cathode materials.

Planar strain driven by constituent element variations

Both NCFMT and NCFMS were carefully synthesized through a conventional solid-state method. The compositions of cathode material were verified by inductively coupled plasma–atomic emission spectroscopy, as shown in Supplementary Table 1. X-ray diffraction (XRD) patterns of the two compounds were collected, as shown in Fig. 1a. The diffraction peaks of the two XRD patterns can be well identified as an O3-type layered structure with an *R*-3*m* symmetry. However, there are noticeable differences in their peak shapes. NCFMS exhibits an obvious anisotropic diffraction peak broadening, with larger full-width at half-maximum in peaks with more *a*–*b* axis character (larger angle to the (003) plane) when compared with the (00*l*) diffraction peaks. This indicates severe lattice distortion or strain within the long-range ordering *ab* plane due to the mismatch of ion size, mass and valence-electron configuration. In contrast, NCFMT has extremely sharp diffraction peaks. Scanning electron microscopy images show that both cathodes have an elliptical ball-shaped grain morphology with an average size of approximately 2–3 μm (Supplementary Fig. 1), ruling out crystallite size effects on XRD peak broadening. A typical Williamson–Hall analysis was conducted to gain more insights (Fig. 1b)[24]. The calculation details of lattice strain ε are presented in Methods and Supplementary Tables 2 and 3. For the NCFMS sample, the lattice strain is higher within the *ab* plane (0.51%) than between the *ab* planes (0.15% along the *c* axis), indicating stronger interactions between TM ions than between TM ions and Na^+, thus leading to enhanced cation displacements from high-symmetry sites (Fig. 1c). In contrast, NCFMT has an overall lattice strain of only 0.01%, indicating a well arranged atomic configuration with minimal ionic displacement (Fig. 1c).

Rietveld refinement of XRD patterns (Supplementary Fig. 2 and Supplementary Tables 4 and 5) revealed slightly higher lattice parameters for NCFMS ($a = b = 3.01$ Å, $c = 16.02$ Å) than for NCFMT ($a = b = 2.99$ Å, $c = 15.99$ Å) due to the larger cation radius of Sn^{4+} (0.69 Å) than of Ti^{4+} (0.61 Å). The corresponding interlayer distance of TMO_2 slabs $d_{(O-TM-O)}$ increases from 2.18 Å to 2.31 Å (Supplementary Table 6), further confirming the local elemental interaction in NCFMS sample. The striking difference between the large (Sn^{4+} $4d^{10}$ configuration) and small (Mn^{4+} $3d^3$ configuration) components within the same TMO_2 slab of NCFMS leads to TMO_6 octahedron expansion and contraction, respectively, both of which can generate lattice distortion or strain. Despite the variance in the ionic radii of the elements in NCFMT, the expansion caused by large divalent ions and contraction caused by small tetravalent ions in the first row of TMs in the Periodic Table would offset each other through the formation of ion pairs/clusters, such as Ni–Mn, Cu–Ti, Ni–Fe–Mn and so on. These features would result in a more compatible atomic configuration, reducing lattice distortion/strain (Supplementary Fig. 3 and Supplementary Discussion 1).

The cross-sectional HAADF-STEM images (Fig. 1d) show that both materials have a well defined layered structure consisting of stacked Na and TM layers, devoid of any stacking faults that could potentially lead to diffraction peak broadening[25,26]. The atomic-resolution EDS mapping confirms the uniform and random distribution of all five elements within each sample beneath the projected atomic columns.

https://doi.org/10.1038/s41560-024-01616-5

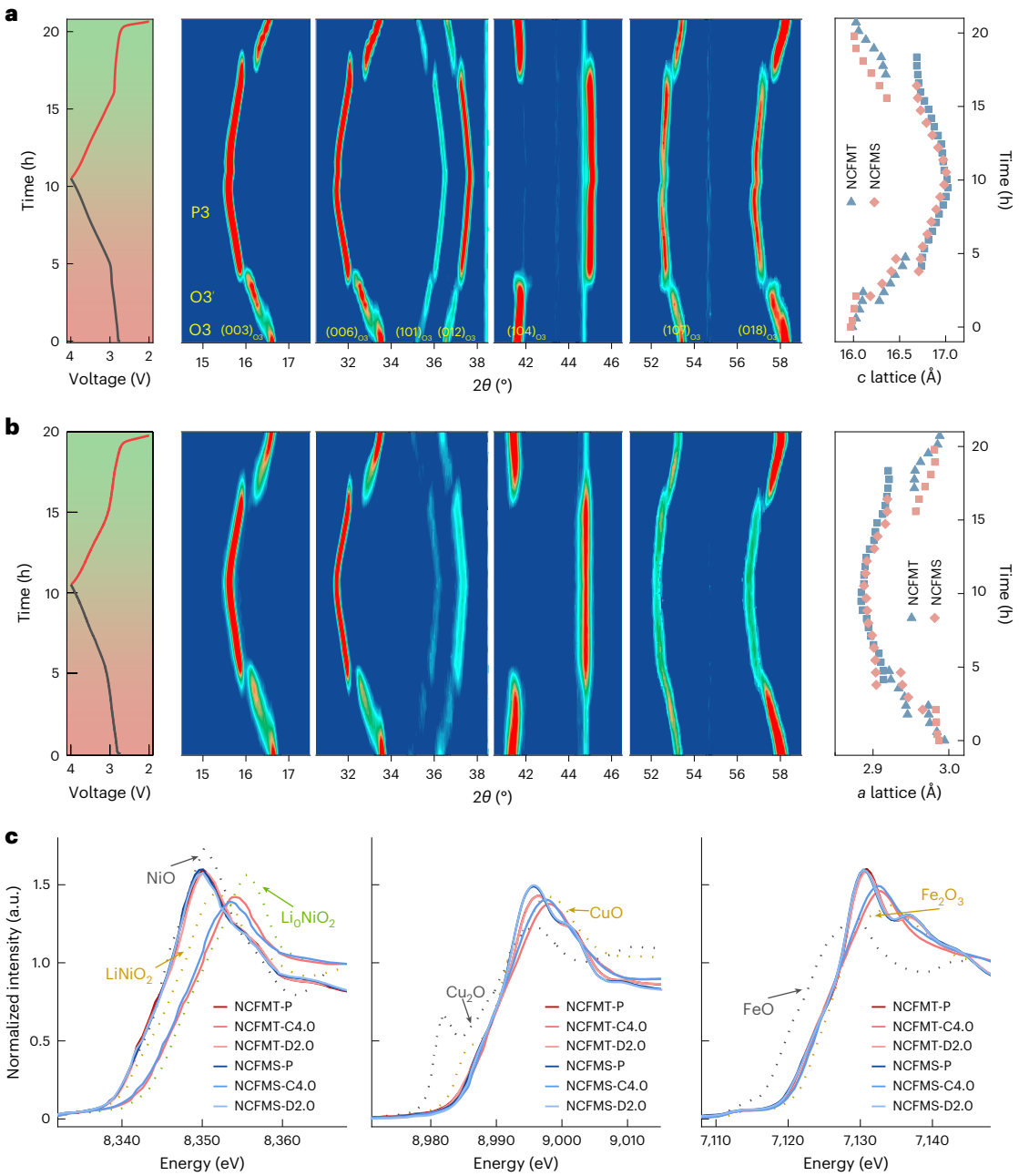

Fig. 3 | Structural characterizations of the NCFMS and NCFMT cathodes. a,**b**, In situ XRD patterns of NCFMS (**a**) and NCFMT (**b**) during first charge and discharge. **c**, X-ray absorption near-edge structure of Ni K, Cu K and Fe K edges of NCFMS and NCFMT during first charge and discharge.

Moreover, no evidence of element aggregation is observed (Supplementary Fig. 4), indicating a perfect local compositional homogeneity.

Electrochemical performance

To reveal the impact of the lattice strain on the electrochemical performance, we constructed half cells with NCFMT and NCFMS as cathodes and conducted all tests at room temperature. The initial galvanostatic charge and discharge profiles of NCFMS and NCFMT within 2.0–4.0 V (Fig. 2a) show that NCFMT has a higher reversible capacity (141.5 mAh g^{-1}) than does NCFMS (129.5 mAh g^{-1}), probably due to the smaller molar mass of Ti when compared with Sn. Meanwhile, NCFMT exhibits a superior initial Coulombic efficiency of 95%, much better than that of 88% for the NCFMS, suggesting the outstanding reversibility and fewer side-reactions of the NCFMT cathode. Normalized rate capability comparison (Fig. 2b) reveals that strain-free NCFMT not only delivers higher discharge specific capacities at all rate currents, but also shows much improved normalized capacity retentions when compared with NCFMS. For example, at a 5 *C* rate current, NCFMT achieves a specific discharge specific capacity of 120 mAh g^{-1} with 86% capacity retention, evidently higher than the 76 mAh g^{-1} and 59% in NCFMS, also surpassing previously reported O3-type cathodes (Fig. 2c)[11,13,27–29]. Galvanostatic intermittent titration technique measurements in Supplementary Fig. 5 show that NCFMT exhibits smaller voltage polarization than NCFMS, and the Na^+ transport in the NCFMT electrode is nearly twice as fast as in the NCFMS electrode, indicating efficient redox kinetics and ionic transport channels owing to the stable structural framework. Furthermore, strain-free NCFMT also demonstrates remarkable cycling performance, retaining 85% capacity after 500 cycles at 1 *C* rate current (Fig. 2d), while NCFMS retains only 64% capacity under the same conditions. We further assessed the high-temperature cycling stability

of NCFMT and NCFMS by conducting 1 *C*–1 *C* charge–discharge cycling at 45 °C. NCFMT exhibits stable performance, delivering a discharge specific capacity of 106 mAh g^{-1} with 80% capacity retention after 500 cycles (Fig. 2e), By contrast, NCFMS fails rapidly within 100 cycles. When charged to a higher voltage, the NCFMT cathode also exhibits much better reversible specific capacity and cycling stability when compared with NCFMS (Supplementary Fig. 6). The superior cycling performance of NCFMT is attributed to the high compatibility of its all-3*d* TM components in TMO_2 slabs, which results in reduced lattice strain. This probably mitigates the collective mechanochemical degradation caused by factors such as Jahn–Teller distortion, inhomogeneous desodiation and anisotropic lattice parameter evolution during Na^+ (de)intercalation[8,10,13,30]. This degradation mechanism will be clearly demonstrated in the following sections.

Structural evolution and redox mechanism

The cycle stability of O3-type layered oxides is potentially linked to their structural evolution. To investigate the impact of lattice strain differences on structural properties, in situ XRD experiments were first performed on NCFMT and NCFMS cathodes. The two cathodes experience similar reversible structural transformations, which go through O3–P3–O3 phases (Fig. 3a,b). During Na^+ deintercalation, the (003) peaks shift to lower angles in low-voltage regions due to oxygen plane repulsion, suggesting expansion of the *c* lattice parameter. The (101) and (012) peaks shift to higher angles as active TM oxidation causes a reduction of the TM–O bond and a contraction of the *a*/*b* lattice parameter. Note that a Na-deficient hexagonal O3′ phase appears before the P3 phase transition during charging, avoiding the undesired monoclinic O′3 phase. The P3 to O3 transition is smoother during discharging, consistent with our previous study[13]. Furthermore, lattice parameter variations in the two electrodes are quite consistent. In addition, ex situ X-ray absorption near-edge structure and Fourier-transformed extended X-ray absorption fine structure of the TM were also used to investigate the electronic structural and local structural changes in NCFMT and NCFMS electrodes during the electrochemical process, and the results are presented in Fig. 3c and Supplementary Fig. 7. These results do not reveal any differences in redox mechanism or the degree of redox couples' participation between the two electrodes. Thus, the reason for the distinct capacity degradation behaviours of the two cathodes remains elusive.

Visualizing elemental segregation and its impact

To understand the distinct degradation mechanisms, we further characterized the microstructural evolution of NCFMT and NCFMS samples after 500 charge–discharge cycles within 2.0–4.0 V using STEM. A cross-sectional view (Fig. 4a) shows that cycled NCFMS has a damaged surface with numerous dislocations[31,32], cracks along the (003) lattice fringes and a severe Na^+–TM intermixing rock-salt phase (Fig. 4b), potentially reducing reversible Na^+ intercalation and causing electrochemical degradation. In addition, several bright columns within the cathode particle are observed (Fig. 4c), attributed to Sn ion segregation in TMO_2 slabs due to higher *Z* contrast in HAADF images. The HAADF-STEM image line profile (inset of Fig. 4c) shows that the layered structure was well maintained near bright Sn-rich columns, but the *d* spacing among these columns expanded (from $d = 0.54$ nm to $d = 0.61$ nm), suggesting unoccupied Na-ion sites and increased O–O repulsion. Furthermore, slight lattice gliding among Sn-rich columns is observed (green line in Fig. 4c), indicating a decreased energy barrier for interlayer glide due to reduced residual Na^+ content and increased TM–TM distance mismatch in Sn-rich features. The close-to-atomic EDS map analysis (Fig. 4d) further confirms Sn enrichment in bright columns and a mixture of the other four TM ions in Sn-poor columns, contrasting with the uniform elemental distribution in the pristine sample. A homogeneous O distribution indicates the well maintained cubic oxygen close packing. We also observe an attenuated Na signal between Sn-rich columns, suggesting that the removal of active redox couples from the Sn-rich columns hinders Na^+ intercalation and causes severe structural degradation, which can be considered as another important factor leading to the electrochemical decay. A similar Mg segregation phenomenon was observed in a P2-$Na_{0.67}Ni_{0.23}Mn_{0.67}Mg_{0.1}O_2$ cathode during repeated cycling at higher charging cutoff voltage, while Mg segregation occurs within the Na layers, which could act as robust pillars to mitigate the occurrence of cracks in the structure[30]. The Sn segregation in the interior of NCFMS single-crystal particles is probably a result of TM migration over extended cycling, achieved by simultaneous diffusion of all five elements, which will be discussed in more detail later.

The corresponding geometric phase analysis[33,34] of an area with both Sn-rich and Sn-poor columns (Fig. 4e) revealed the distinct strain distribution between the two domains. Localized lattice strain exhibits tensile stress along the Sn-rich layer, stretching the (003) lattice plane, which will introduce compressive stress in the Sn-poor area, compressing the lattice. This deteriorates Na^+ transport properties, explaining the inferior rate capability of the NCFMS cathode. Additionally, such metastable structure with severe stress fields can cause local rupture of atomic planes during electrochemical cycling. Significant intragranular fractures are indeed observed in another more degraded particle (Supplementary Fig. 8), causing deactivation of Na^+ storage sites, loss of electrode electron conduction and exposure of new surfaces to the electrolyte[8,10,35,36]. This explains the severe structural degradation in the surface region contacting the electrolyte. These findings were consistently observed across randomly selected NCFMS particles (Supplementary Figs. 9–11). Focused ion beam (FIB) sectioning facilitated the detection of elemental segregation and intragranular microcracks within the particles, as these signals are often buried in the interior. Identical characterizations on NCFMT particles show no structural damage (Fig. 4f–h) or elemental segregation (Supplementary Figs. 12,13) after 500 cycles. This demonstrates substantial chemical and structural compatibility among the five first-row 3*d* TMs in a high-entropy configuration, which maximizes structural stabilization.

The structural evolution was further examined by ex situ XRD (Supplementary Fig. 14), which was consistent with the STEM analysis. After 500 cycles, the (00*l*) diffraction peaks in NCFMS show an intense broadening similar to the (*hk*0) peak broadening in the pristine NCFMS, indicating multiple detrimental phase transitions (Sn-rich and Sn-poor regions) accompanying severe stress accumulation. In contrast, the integral diffraction peaks in NCFMT only show a slight broadening after prolonged cycling, indicating suppressed structural evolution.

Strain-induced mechanochemical degradation mechanisms

The inhomogeneous element distribution in the TMO_2 layers of the cycled NCFMS cathode indicates progressive aggregation of not only Sn but also the other four elements with repeated cycling. This occurs despite the low cutoff voltage of 4.0 V, implying that metal-ion migration happens in an integrated face-centred cubic oxygen lattice without substantial oxygen vacancy formation. This differs from the conventional understanding that TM migration in layered oxides is usually accompanied by oxygen ligand release or vacancy formation[37,38]. Here we believe that the localized TMO_6 discrepancy (distortion and displacement) in the TMO_2 layers plays an overwhelming role in triggering the metal-ion migration in NCFMS, which spontaneously adjusts TM rearrangement and leads to elemental segregation during prolonged cycling.

To explore the thermodynamic/kinetic origins of elemental segregation and metal-ion migration, density functional theory (DFT) and bond-valence (BV) calculations were performed. We first focus on the ground-state energies of pristine O3-NCFMT/NCFMS and charged P3-NCFMT/NCFMS with either uniformly distributed (Sn/Ti-unsegregated) or agglomerated (Sn/Ti-segregated) Sn/Ti ions

https://doi.org/10.1038/s41560-024-01616-5

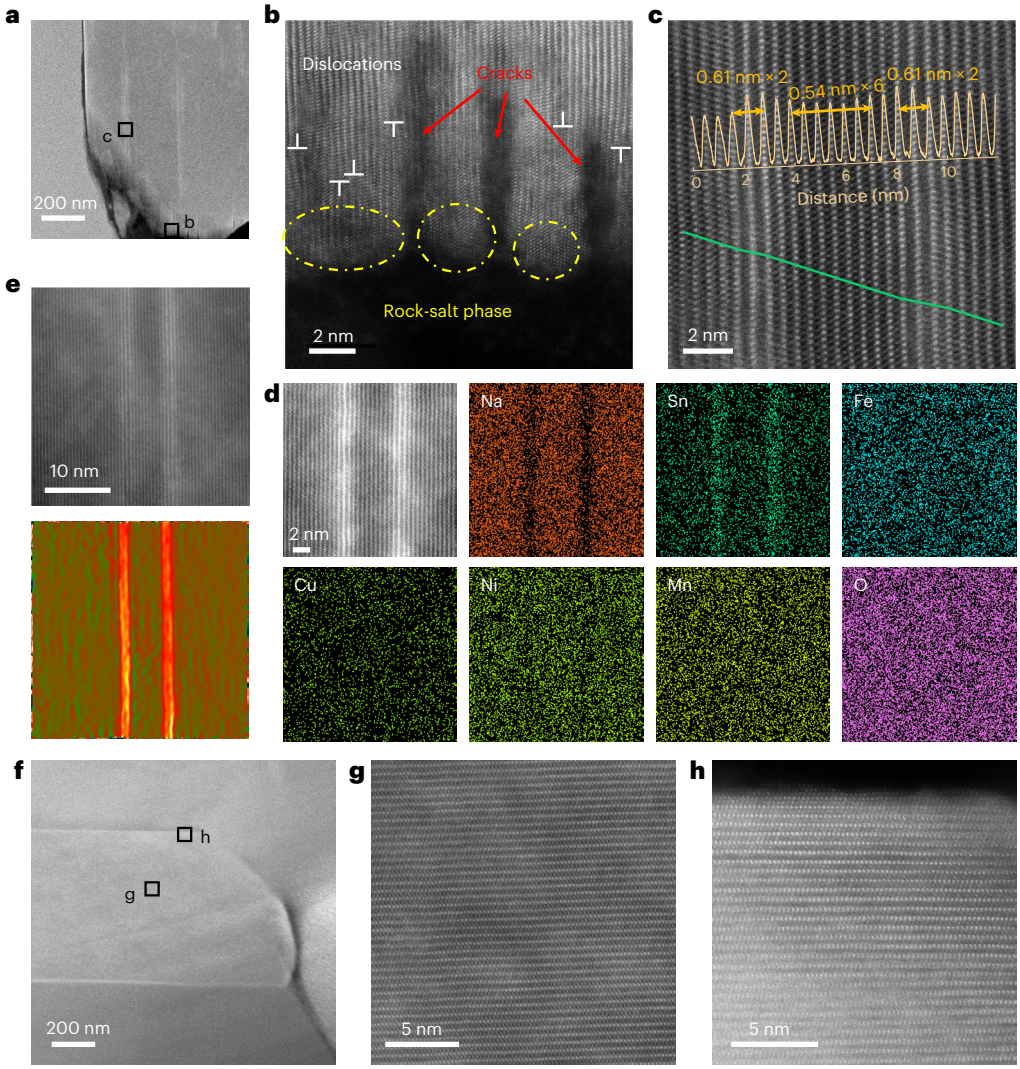

Fig. 4 | Structural characterizations of the cycled NCFMS and NCFMT cathodes. a, Cross-sectional low magnification ADF-STEM image of NCFMS after 500 cycles. **b**,**c**, HAADF-STEM images of cycled NCFMS in **a**. Substantial dislocations are identified in the cycled NCFMS cathode. **d**, EDS mapping of region c in **a**. **e**, Strain state of the element-segregated region obtained by geometric phase analysis. **f**, Cross-sectional low magnification ADF-STEM image of NCFMT after 500 cycles. **g**,**h**, HAADF-STEM images of cycled NCFMT in **f**.

on the basis of DFT calculations. In the calculations for O3-NCFMT/NCFMS, Sn/Ti-unsegregated structures were created by randomly and uniformly placing metal ions into TMO_2 slabs, while for the Sn/Ti-segregated structures Sn/Ti ions in the same layer cluster together to form dimers (Supplementary Fig. 15). To model the discharged P3 structures, the TM distributions arranged in O3 structures were retained and multiple in-plane Na/vacancy orderings were introduced in the NaO_2 slab with approximately 0.56 Na ions removed according to the electrochemistry results. The resulting relative energies in Fig. 5a identify that both O3- and P3-type Sn-containing samples exhibited an energy reduction when transitioning from a homogeneous elemental distribution to Sn aggregation. In particular, an energy change of −19.1 meV per atom was found in P3 structures, suggesting a strong energetic driving force for formation of Sn-segregated layered structure in the desodiated state. In addition, we can also infer that the pristine O3-NCFMS material with uniform elemental distribution as identified by STEM-EDS was metastable (5.4 meV higher than Sn-segregated sample), although it could reach the thermodynamic equilibrium state at the synthesis temperature due to the entropy stabilization effect ($\Delta G = \Delta H - T\Delta S$). This reinforces the conclusion that lattice distortion/strain exists within the *ab* plane of NCFMS when it returns to the ambient temperature due to the chemical incompatibility of the Sn ion with the other four constituent elements. In sharp contrast, Ti-containing samples with homogeneous element distributions were the lowest in energy when compared with the Ti-segregated configurations regardless of O3 or P3 structure (Fig. 5b), guaranteeing better reversibility of the electrode reaction.

During the charging process, redox-active TMs such as Ni^{2+}, Cu^{2+} and Fe^{3+} undergo oxidation reaction; for example, Ni^{2+} transforms to Ni^{3+}. This, along with the structure evolution from O3 to P3 phase, shortens the Ni–O bonding length, suggesting that ligand oxygen ions are dragged towards active Ni^{3+}, thus causing oxygen displacement (Fig. 5c). In fact, when the Ni^{3+} is mainly second-coordinated by redox-inactive TM (especially the Sn^{4+}), the oxygen displacement will be suppressed due to the stabilization effect of chemically stiff Sn–O bonds or SnO_6 octahedron units, which will result in undercoordinated Ni^{3+}. Considering the intrinsic lattice strain in the TMO_2 slabs, it is more favourable for Ni^{3+} to move to triangular prism sites in the Na layer through a shared triangle[38]. The alternative route to the tetrahedral sites in the TMO_2 layers is unfavourable due to strong face-sharing electrostatic interactions. Furthermore, severe lattice microstrain in excessively extended TMO_2 slabs of the NCFMS cathode may facilitate

https://doi.org/10.1038/s41560-024-01616-5

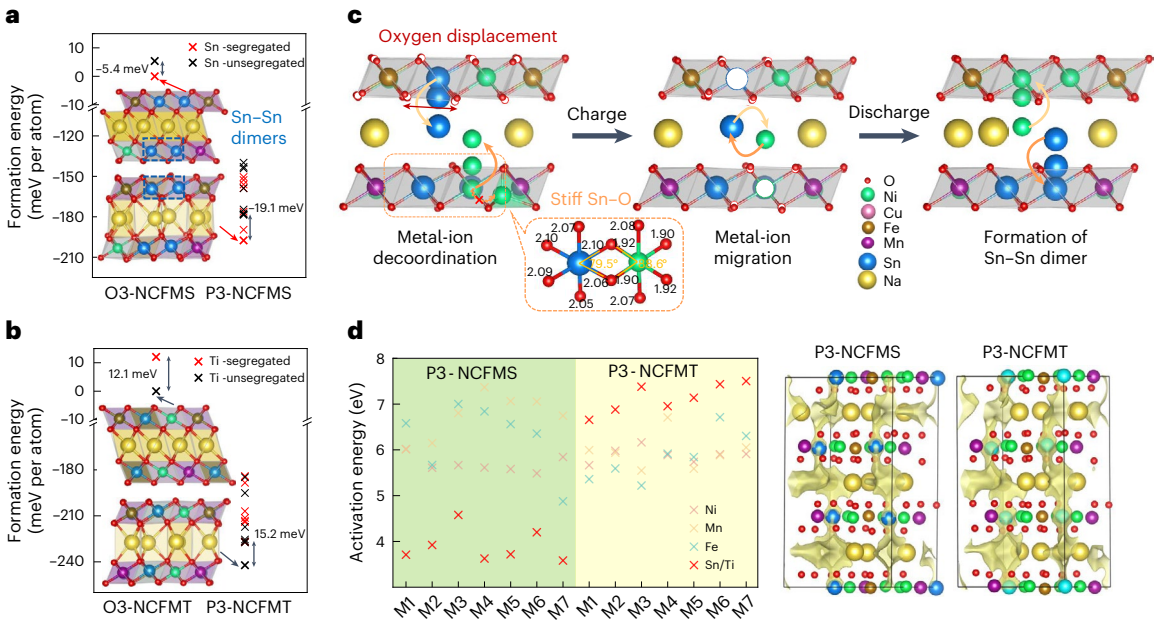

Fig. 5 | Sn segregation in the interior of NCFMS single-crystal particles. **a**,**b**, Calculated total energies for O3/P3-$Na_{27-x}Ni_{12}Fe_3Mn_6Sn_6O_{54}$ and O3/P3-$Na_{27-x}Ni_{12}Fe_3Mn_6Ti_6O_{54}$ with and without elemental segregation from DFT. Insets: corresponding crystal structures. **c**, Illustration of Sn migration and Sn–Sn dimer formation in P3-NCFMS. **d**, Activation energy of Ni, Mn, Fe, Sn and Ti for multiple configurations, and the pathways connecting Sn and Ti ions. The pathways connecting Ni, Fe and Mn ions are very similar to those connecting Sn and Ti ions, hence they are not shown.

this process. We note that the empty NiO_6 octahedron will remain more spacious due to the loss of Ni–O attraction. Conversely, when the Sn^{4+} is mainly second-coordinated by redox-active TM, the driving force of oxygen displacement induced by redox-active TM oxidation will ultimately dominate and inevitably cause expansion of the SnO_6 octahedron unit, which consequently destabilizes the original site and induces the thermodynamically driven Sn migration. This migration leads to the contraction of the empty octahedral sites. Upon Na^+ intercalation, it is thermodynamically favourable for Sn^{4+} to migrate to the empty expanded NiO_6 octahedral site, leading to formation of the interlayer Sn–Sn dimer, whereas Ni^{3+} will migrate to the original site of Sn^{4+} due to a similarly energetically favourable local environment.

The migration of metal ions along triangular prism sites in the Na layer is believed to be feasible due to the relatively weak electrostatic repulsion with cations in the TMO_2 layers. However, this may lead to a metastable state because of the size mismatch between metal ions and the spacious prismatic sites within the P3 structure[39]. This mismatch provides a rationale for why, where migration has occurred on the surface of the particles, metal ions often preferentially escape and dissolve into the electrolyte, as evidenced in Supplementary Table 7. This dissolution phenomenon becomes increasingly thermodynamically favourable at higher temperatures, consequently accelerating capacity fade (Fig. 2e). Moreover, the formation of localized Sn–Sn dimers and substantial local environment changes for nearby redox-active TMs will further aggravate this interchangeable metal-ion migration. Furthermore, we infer that the dynamic migration of nearby redox-inactive Mn^{4+} species is triggered due to the increased localized lattice strain. As a result, accumulative Sn-rich columns are formed over extended cycling, in accordance with the Schelling model (Supplementary Fig. 16 and Supplementary Discussion 2) and previous findings of cation aggregation in perovskite films[40]. In the case of the NCFMT cathode, metal-ion migration is suppressed, preventing Ti-rich region formation and stabilizing the crystal structure. To further reveal the differential behaviour of metal-ion migration in NCFMT and NCFMS, we used the BV method to obtain the possible transportation channels and corresponding activation energies of various metal ions. As shown in Fig. 5d, the continuous three-dimensional pathways connecting TM ions are formed between two adjacent TMO_2 layers by multiple triangular prism sites in the Na layer. By comparing the activation energies of multiple metal ions, we find that it would cost the minimum energy for Sn ions to penetrate the TMO_2 and NaO_2 layers, whereas it would cost the maximum energy for Ti ions to travel throughout the lattice along these pathways. Therefore, the Sn ions are prone to cluster together with the lowest energy barrier, leading to Sn enrichment in NCFMS at desodiated states. The above results demonstrate that the high compatibility of constituent elements (all 3*d* TM) plays a vital role in securing better structural reversibility and energy retention for high-entropy layered oxide cathodes. A spontaneous migration of Ti^{4+} cations from TMO_2 layer octahedral sites to Li layer tetrahedral interstices in the $Li_2Ru_{0.75}Ti_{0.25}O_3$ structure (4*d* TM dominant matrix)[41] can also be well explained by the compatibility principle.

Mechanochemical compatibility of constituent elements

To further validate our hypothesis, $NaNi_{0.3}Mg_{0.1}Fe_{0.2}Mn_{0.3}Ti_{0.1}O_2$ (NMFMT), $NaNi_{0.3}Zn_{0.1}Fe_{0.2}Mn_{0.3}Ti_{0.1}O_2$ (NZFMT) and $NaNi_{0.3}Cu_{0.1}Fe_{0.2}Mn_{0.3}Zr_{0.1}O_2$ (NCFMZ) cathodes were also examined (Supplementary Figs. 17 and 18). According to the XRD patterns (Supplementary Fig. 17), all materials had obvious impurity phases besides the O3 structure, such as cubic MgO (space group *Fm*-3*m*, Powder Diffraction File (PDF) 45-946) in NMFMT, hexagonal ZnO (space group *P*63*mc*, PDF 36-1451) in NZFMT and monoclinic Na_2ZrO_3 (space group *A*2/*a*, PDF 35-770) in NCFMZ. This indicates that Mg^{2+} and Zr^{4+} have a poor compatibility with the rest of the 3*d* TMs owing to differences in size, mass and valence-electron configuration, leading to elemental aggregation and further phase segregation early in the synthetic process, which triggers the microstrain release but reduces configuration entropy. In contrast, a slight ZnO phase segregation in NZFMT occurs because the zinc is four-coordinated by oxygen in the zincite structure, giving a rising value for the enthalpy of solution of ZnO into the O3 framework[42], leading to reduced solid solution. As expected, electrochemical results (Supplementary Fig. 19) show that the NZFMT cathode delivers much better reversible specific

https://doi.org/10.1038/s41560-024-01616-5

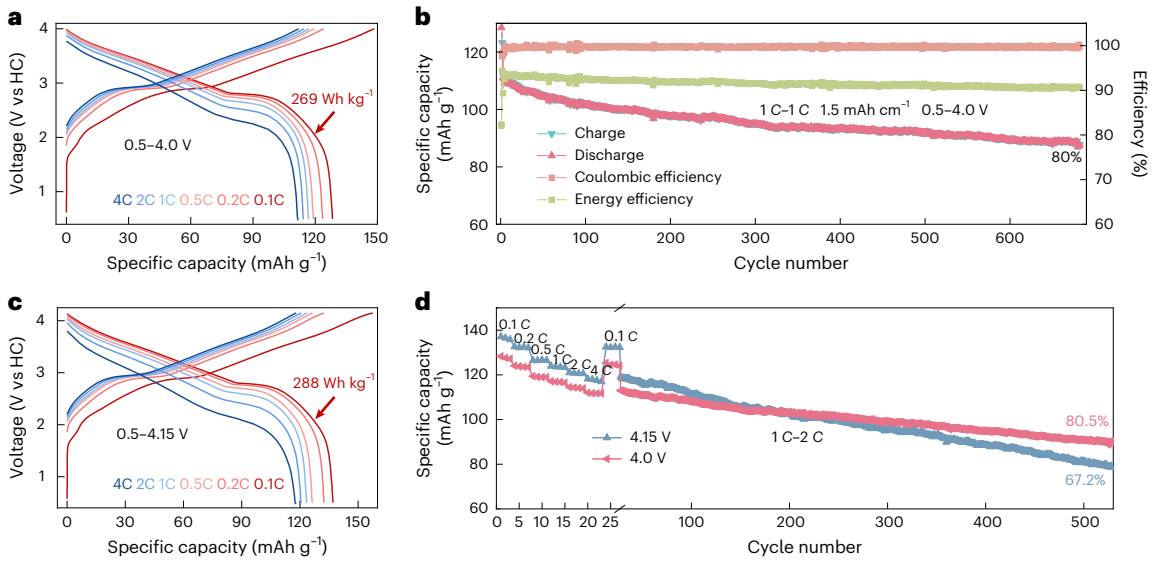

Fig. 6 | Full-cell performance of NCFMT//HC in different voltage ranges. **a**, Charge–discharge profile at 0.1 *C*, 0.2 *C*, 0.5 *C*, 1 *C*, 2 *C* and 4 *C* within a voltage range of 0.5–4.0 V. **b**, Cycling performance at a current rate of 1 *C* and a cutoff potential of 4.0 V. **c**, Charge–discharge profile at 0.1 *C*, 0.2 *C*, 0.5 *C*, 1 *C*, 2 *C* and 4 *C* within a voltage range of 0.5–4.15 V. **d**, Rate capability at cutoff potentials of 4.0 and 4.15 V. Here, specific capacity is calculated on the basis of cathode active mass.

capacity and capacity retention when compared with the other two cathodes, second only to NCFMT. Thus, these results confirm that the high compatibility of the isoperiodic element in layered cathodes might play a crucial role in the structural stability during extended cycling, which can be further applied in various cathode materials. Furthermore, Supplementary Figs. 20 and 21 show that the prepared quaternary all-3*d* TM oxide cathodes, which can be categorized as medium-entropy oxides with slight lattice strain, delivered inferior capacity retention. This highlights the feasibility and necessity of the entropy-dominated phase stabilization effect for enhancing the energy storage performance of layered cathodes.

We further fabricated a full cell based on an NCFMT cathode and hard carbon (HC) anode, as shown in Fig. 6a, which delivered an energy density of 269 Wh kg^{-1} (on the basis of the total mass of active materials) at 0.1 *C* with Coulombic efficiency of 86%, slightly higher than in our recent report[43]. The full cells achieved an impressive long-term cycling stability during the 1 *C*–1 *C* charge–discharge process (Fig. 6b), retaining 80% of their initial specific capacity after 682 cycles with high Coulombic efficiency and a remarkable average energy efficiency of ~91%. To the best of our knowledge, this stability performance is among the best coin full cells based on O3 layered structure (Supplementary Table 8). In addition, full cells charged to higher cutoff voltages (4.15 V) at different rates (Fig. 6c,d, half-cell performance is shown in Supplementary Fig. 22) were also characterized to assess the potential for increasing the system's energy density, despite showing a slightly faster capacity decay after a rate test when compared with those cycled within 4.0 V, which can be further improved through electrolyte optimization[44].

Conclusion

In this work, we reveal the critical role of high compatibility among constituent elements in securing better structural reversibility and energy retention in high-entropy layered cathodes. By comparing two analogous materials with distinct lattice microstrains, we demonstrate that the notable microstrain observed in the NCFMS cathodes, primarily localized in the *ab* plane, is a result of metal-ion displacement caused by differences in atomic size, mass and valence-electron configuration between Sn^{4+} and other 3*d* TM ions. Our findings reveal a strain-induced mechanochemical degradation mechanism in the NCFMS cathode, where local planar strain along with lattice strain induced by active TM redox reactions promotes metal-ion migration, leading to Sn segregation in the bulk and metal-ion dissolution at the surface, ultimately deactivating cathode particles. In contrast, NCFMT exhibits notably improved electrochemical performance when compared with NCFMS and other medium-/high-entropy layered cathodes. Its high energy density and good cycling stability are attributed to the high mechanochemical compatibility of its constituent elements in the TMO_2 slabs. Our study underscores the significance of careful elemental selection in creating high-performance high-entropy cathode materials. These new insights open a promising avenue for the rational optimization of high-entropy oxide cathode compositions and provide robust design guidelines for developing long-life layered oxide cathodes for commercial applications in NIBs.

Methods

Synthesis

All of the target cathode materials were synthesized by a routine solid-state reaction method. The theoretical stoichiometric ratio of Na_2CO_3 (Alfa, 99.5%), NiO (Aladdin, 99.9%), CuO (Aladdin, 99.9%), MgO (Aladdin, 99.5%), ZnO (Aladdin, 99.5%), Fe_2O_3 (Aladdin, 99.9%), MnO_2 (Aladdin, 98%), TiO_2 (Aladdin, 99.5%), ZrO_2 (Aladdin, 98%) and SnO_2 (Aladdin, 98%) was mixed carefully in an agate mortar. 2% more Na_2CO_3 was added to compensate for possible loss in the high-temperature calcination process. Subsequently all of the mixtures were sintered at 900 °C for 15 h in a muffle furnace. Finally, the cathode materials were cooled to 120 °C slowly in the furnace and transferred to an glovebox without exposure to air.

Electrochemical characterization

Cathode films were fabricated by mixing 80 wt% active compound, 10 wt% carbon nanotubes and 10 wt% polytetrafluoroethylene inside a glovebox. The mixtures were rolled to form self-standing films; the loading mass of the active material was 8–10 mg cm^{-2}. The anode was fabricated by spreading a slurry of HC (HiNa) material, acetylene black and sodium alginate binder (in a weight ratio of 92:4:4) on Al foil for full cells; the loading mass of anode active materials was kept at ~4 mg cm^{-2}. The fabricated electrode films were dried at 120 °C under vacuum overnight. Finally, they were assembled into CR2032-type coin cells in an argon-filled glovebox (H_2O and O_2 of <0.1 ppm). Note that a carbon-coated Al foil was placed between the cathode film and

stainless-steel spacer to achieve better electronic conductance. Glass fibre (Whatman GF/A) served as the separator and Na metal or HC was utilized as counter- or reference electrode. 1 M $NaClO_4$ in propylene carbonate–ethylene carbonate–dimethyl carbonate (PC/EC/DMC = 1:1:1 by volume) with fluoroethylene carbonate (2% by volume) was employed as the electrolyte. In full cells, the weight ratio of the two electrodes was balanced with reference to the charge capacity of the cathode and the discharge capacity of the anode during the first cycle in half cells (a margin of error of less than 2%). Galvanostatic charge–discharge tests of the half cells were conducted on Landt battery test systems (CT2001A) or Neware battery test systems (CT-4008T) in voltage ranges of 2.0–4.0/4.1/4.15/4.2/4.3/4.5 V at room temperature (25 °C) or 45 °C. The full cells were tested in the voltage range of 0.5-4.0 V or 0.5-4.15 V. The galvanostatic intermittent titration technique was conducted by applying a titration step at 0.1 *C* of 20 min and a relaxation step of 3 h.

Calculation of Na^+ diffusion coefficients through galvanostatic intermittent titration technique results. As the Na^+ diffusion/transportation in the electrode materials fits Fick's second law, the apparent Na^+ diffusion/transportation coefficients (D_{Na+}) in the one-phase regions can be evaluated using

$$D_{Na^+} = \frac{4}{\pi\tau}\left(\frac{m_B V_M}{M_B S}\right)^2\left(\frac{\Delta E_S}{\Delta E_\tau}\right)^2 \quad (\tau \ll L^2/D) \tag{1}$$

where m_B is the mass of the cathode active material, V_M represents the molar volume of the material, M_B is the molecular weight of the material, S is the surface area between electrolyte and electrode, ΔE_S is the difference of the steady-state voltage of the cell during the rest and ΔE_τ is the transient voltage difference of the cell during applied current within time τ. τ is the time duration for which the current is applied, and L is the diffusion distance of Na^+ from lattice to liquid electrolyte.

Material characterization

The structural features of the as-prepared compounds were first investigated by XRD measurement (Bruker-AXS D8 Advance instrument with Cu Kα X-ray source). The XRD data were fitted and then refined using FullProf suite software. The elemental compositions of the cathode materials were verified by inductively coupled plasma–atomic emission spectroscopy (Shimadzu, ICPS-8100). For metal-ion dissolution measurements, the cells were disassembled in a glovebox, and the separators were extracted and soaked in 2 ml of 2 M HCl aqueous solution. After ultrasound treatment for half an hour, solutions were further diluted with deionized water to a final volume of 10 ml. Finally, the supernatant was used for the inductively coupled plasma–atomic emission spectroscopy test. Scanning electron microscopy measurements were conducted using a Hitachi S-4800 (10–15 kV). Atomic-resolution HAADF-STEM images and EDS mappings were collected on a JEM-ARM200F NEOARM microscope equipped with a JEOL's EDS detector at an acceleration voltage of 200 kV. To investigate the bulk structure of the cathode materials, cross-sectional samples were fabricated through a focused ion beam–scanning electron microscopy dual-beam system. A homemade Swagelok cell for in situ XRD measurements was assembled with carbon-coated Al foil as the current collector and X-ray window. X-ray absorption spectroscopy was conducted on the 1W1B beamline of Beijing Synchrotron Radiation Facility. The X-ray energy for each edge was calibrated by using the corresponding metal foils. The X-ray absorption spectra were normalized and the background removed with the program IFEFFIT. The charged/discharged samples were prepared electrochemically.

Williamson–Hall analysis

It is known that the broadening of the diffraction peaks in the sample's XRD pattern can be ascribed to crystallite size and microstrain, which vary differently as a function of Bragg angle (θ) and can be calculated using the following equation:

$$\beta_{size} = \frac{K\lambda}{L\cos\theta} \tag{2}$$

$$\beta_{strain} = 4\varepsilon\frac{\sin\theta}{\cos\theta} \tag{3}$$

where β_{size} and β_{strain} are crystallite size and strain broadening, respectively, K is a constant depending on crystallite shape (here defined as 0.9), λ is the wavelength of the X-ray source, L represents the crystallite size and ε is the lattice microstrain. The instrumental broadening can be corrected by the standard sample of single-crystal silicon using the following equation:

$$\beta_{total}^2 = \beta_{instrument}^2 + \beta_{sample}^2 \tag{4}$$

where β_{total} is the measured full-width at half-maximum of each peak, $\beta_{instrument}$ is the instrumental broadening (here 0.05727°) and β_{sample} is the real sample full-width at half-maximum.

The Williamson–Hall method assumes that β_{sample} is a simple sum of β_{size} and β_{strain}, using the following equation:

$$\beta_{sample} = \beta_{size} + \beta_{strain} = \frac{K\lambda}{L\cos\theta} + 4\varepsilon\frac{\sin\theta}{\cos\theta}. \tag{5}$$

Multiplying throughout by $\cos\theta$ gives

$$\beta_{sample}\cos\theta = \frac{K\lambda}{L} + 4\varepsilon\sin\theta. \tag{6}$$

Therefore, ε can be extracted from the slope value of the plot of $\beta_{sample}\cos\theta$ versus $4\sin\theta$. The XRD patterns were fitted to a Lorentzian distribution function. The calculation details of ε are presented in Supplementary Tables 2 and 3.

First-principles calculations

In this work, we carried out DFT calculations using the Vienna Ab initio Simulation Package[45,46] with the Perdew–Burke–Ernzerhof[47] generalized gradient approximation[48]. Hubbard U potential correction was used to take into account the electronic correlation effects of TM 3*d* electrons in Ni (5.2 eV), Fe (4.9 eV), Mn (5.0 eV)[49] and Ti (4.2 eV)[50] ions. In the DFT calculations, the energy cutoff of 500 eV was employed, and ions were fully relaxed in the optimization process under the energy and force convergence criteria of 10^{-6} eV and 0.02 eV $Å^{-1}$, respectively. The quasiempirical BV method[51,52] was performed to obtain the possible ionic transportation channels and migration energy barriers of TM ions.

For convenience in the theoretical simulation, two model systems, O3-$Na_{27}Ni_{12}Fe_3Mn_6Sn_6O_{54}$ (representing NCFMS) and O3-$Na_{27}Ni_{12}Fe_3Mn_6Ti_6O_{54}$ (representing NCFMT), were used to examine the energetics when TM ions are uniformly distributed or agglomerated (mainly Ti/Sn segregated). We note that the absence of Cu has little impact on the overall energy of these oxides except for configurational entropy, due to the similar structural and electronic features of Cu and Ni ions. Meanwhile, the charged materials P3-$Na_{12}Ni_{12}Fe_3Mn_6Sn_6O_{54}$ and P3-$Na_{12}Ni_{12}Fe_3Mn_6Ti_6O_{54}$ with seven different in-plane Na ordering/disordering configurations were modelled.

To calculate the energy change between the model structures with homogeneous elemental distribution or elemental aggregation, the O3 structure with the lowest ground-state energy was used as energy reference (E_{ref}), here O3-$Na_{27}Ni_{12}Fe_3Mn_6Sn_6O_{54}$ with elemental aggregation and O3-$Na_{27}Ni_{12}Fe_3Mn_6Ti_6O_{54}$ with homogeneous elemental distribution, and the relative formation energies of other models were calculated as $E - E_{ref}$.

Data availability

The data supporting the findings of this study are available within the article and its Supplementary Information files.

References

1. Rudola, A., Sayers, R., Wright, C. J. & Barker, J. Opportunities for moderate-range electric vehicles using sustainable sodium-ion batteries. *Nat. Energy* **8**, 215–218 (2023).
2. Hu, Y.-S. & Li, Y. Unlocking sustainable Na-ion batteries into industry. *ACS Energy Lett.* **6**, 4115–4117 (2021).
3. Zhao, C. et al. Rational design of layered oxide materials for sodium-ion batteries. *Science* **370**, 708–711 (2020).
4. Rudola, A. et al. Commercialisation of high energy density sodium-ion batteries: Faradion's journey and outlook. *J. Mater. Chem. A* **9**, 8279–8302 (2021).
5. Liang, X., Hwang, J. & Sun, Y. Practical cathodes for sodium-ion batteries: who will take the crown? *Adv. Energy Mater.* **13**, 2301975 (2023).
6. Liu, J., Kan, W. H. & Ling, C. D. Insights into the high voltage layered oxide cathode materials in sodium-ion batteries: structural evolution and anion redox. *J. Power Sources* **481**, 229139 (2021).
7. Zheng, J., Ye, Y. & Pan, F. 'Structure units' as material genes in cathode materials for lithium-ion batteries. *Natl Sci. Rev.* **7**, 242–245 (2020).
8. Yu, T., Ryu, H., Han, G. & Sun, Y. Understanding the capacity fading mechanisms of O3-type $Na[Ni_{0.5}Mn_{0.5}]O_2$ cathode for sodium-ion batteries. *Adv. Energy Mater.* **10**, 2001609 (2020).
9. Xu, G.-L. et al. Native lattice strain induced structural earthquake in sodium layered oxide cathodes. *Nat. Commun.* **13**, 436 (2022).
10. Li, Y. et al. Degradation by kinking in layered cathode materials. *ACS Energy Lett.* **6**, 3960–3969 (2021).
11. Song, J. et al. Controlling surface phase transition and chemical reactivity of O3-layered metal oxide cathodes for high-performance Na-ion batteries. *ACS Energy Lett.* **5**, 1718–1725 (2020).
12. Guo, S., Li, Q., Liu, P., Chen, M. & Zhou, H. Environmentally stable interface of layered oxide cathodes for sodium-ion batteries. *Nat. Commun.* **8**, 135 (2017).
13. Ding, F. et al. Using high-entropy configuration strategy to design Na-ion layered oxide cathodes with superior electrochemical performance and thermal stability. *J. Am. Chem. Soc.* **144**, 8286–8295 (2022).
14. Zhao, C., Ding, F., Lu, Y., Chen, L. & Hu, Y. High-entropy layered oxide cathodes for sodium-ion batteries. *Angew. Chem. Int. Ed.* **59**, 264–269 (2020).
15. Fu, F. et al. Entropy and crystal-facet modulation of P2-type layered cathodes for long-lasting sodium-based batteries. *Nat. Commun.* **13**, 2826 (2022).
16. Yao, L. et al. High-entropy and superstructure-stabilized layered oxide cathodes for sodium-ion batteries. *Adv. Energy Mater.* **12**, 2201989 (2022).
17. Zhang, R. et al. Compositionally complex doping for zero-strain zero-cobalt layered cathodes. *Nature* **610**, 67–73 (2022).
18. Zhang, R. et al. Long-life lithium-ion batteries realized by low-Ni, Co-free cathode chemistry. *Nat. Energy* **8**, 695–702 (2023).
19. Jiang, B. et al. High-entropy-stabilized chalcogenides with high thermoelectric performance. *Science* **371**, 830–834 (2021).
20. Yang, B. et al. High-entropy enhanced capacitive energy storage. *Nat. Mater.* **21**, 1074–1080 (2022).
21. Yang, B. et al. Engineering relaxors by entropy for high energy storage performance. *Nat. Energy* **8**, 956–964 (2023).
22. Ding, Q. et al. Tuning element distribution, structure and properties by composition in high-entropy alloys. *Nature* **574**, 223–227 (2019).
23. Oses, C., Toher, C. & Curtarolo, S. High-entropy ceramics. *Nat. Rev. Mater.* **5**, 295–309 (2020).
24. Williamson, G. K. & Hall, W. H. X-ray line broadening from filed aluminium and wolfram. *Acta Metall.* **1**, 22–31 (1953).
25. Luo, D. et al. A Li-rich layered oxide cathode with negligible voltage decay. *Nat. Energy* **8**, 1078–1087 (2023).
26. House, R. A. et al. Superstructure control of first-cycle voltage hysteresis in oxygen-redox cathodes. *Nature* **577**, 502–508 (2020).
27. Yao, H.-R. et al. Designing air-stable O3-type cathode materials by combined structure modulation for Na-ion batteries. *J. Am. Chem. Soc.* **139**, 8440–8443 (2017).
28. Xiao, Y. et al. Exposing {010} active facets by multiple-layer oriented stacking nanosheets for high-performance capacitive sodium-ion oxide cathode. *Adv. Mater.* **30**, 1803765 (2018).
29. Ding, F. et al. A novel Ni-rich O3-$Na[Ni_{0.60}Fe_{0.25}Mn_{0.15}]O_2$ cathode for Na-ion batteries. *Energy Storage Mater.* **30**, 420–430 (2020).
30. Wang, K. et al. Dopant segregation boosting high-voltage cyclability of layered cathode for sodium ion batteries. *Adv. Mater.* **31**, 1904816 (2019).
31. Singer, A. et al. Nucleation of dislocations and their dynamics in layered oxide cathode materials during battery charging. *Nat. Energy* **3**, 641–647 (2018).
32. Yan, P. et al. Intragranular cracking as a critical barrier for high-voltage usage of layer-structured cathode for lithium-ion batteries. *Nat. Commun.* **8**, 14101 (2017).
33. Hüe, F., Hÿtch, M., Bender, H., Houdellier, F. & Claverie, A. Direct mapping of strain in a strained silicon transistor by high-resolution electron microscopy. *Phys. Rev. Lett.* **100**, 156602 (2008).
34. Zhu, Y., Ophus, C., Ciston, J. & Wang, H. Interface lattice displacement measurement to 1 pm by geometric phase analysis on aberration-corrected HAADF STEM images. *Acta Mater.* **61**, 5646–5663 (2013).
35. Lee, S., Su, L., Mesnier, A., Cui, Z. & Manthiram, A. Cracking vs. surface reactivity in high-nickel cathodes for lithium-ion batteries. *Joule* **7**, 2430–2444 (2023).
36. Usiskin, R. et al. Fundamentals, status and promise of sodium-based batteries. *Nat. Rev. Mater.* **6**, 1020–1035 (2021).
37. Csernica, P. M. et al. Persistent and partially mobile oxygen vacancies in Li-rich layered oxides. *Nat. Energy* **6**, 642–652 (2021).
38. Liu, T. et al. Origin of structural degradation in Li-rich layered oxide cathode. *Nature* **606**, 305–312 (2022).
39. Rong, X. et al. Structure-induced reversible anionic redox activity in Na layered oxide cathode. *Joule* **2**, 125–140 (2018).
40. Bai, Y. et al. Initializing film homogeneity to retard phase segregation for stable perovskite solar cells. *Science* **378**, 747–754 (2022).
41. Sathiya, M. et al. Origin of voltage decay in high-capacity layered oxide electrodes. *Nat. Mater.* **14**, 230–238 (2015).
42. Davies, P. K. & Navrotsky, A. Thermodynamics of solid solution formation in NiO–MgO and NiO–ZnO. *J. Solid State Chem.* **38**, 264–276 (1981).
43. Ding, F. et al. Tailoring electronic structure to achieve maximum utilization of transition metal redox for high-entropy Na layered oxide cathodes. *J. Am. Chem. Soc.* **145**, 13592–13602 (2023).
44. Jin, Y. et al. Low-solvation electrolytes for high-voltage sodium-ion batteries. *Nat. Energy* **7**, 718–725 (2022).
45. Kresse, G. & Furthmüller, J. Efficiency of ab-initio total energy calculations for metals and semiconductors using a plane-wave basis set. *Comp. Mater. Sci.* **6**, 15–50 (1996).
46. Kresse, G. & Furthmüller, J. Efficient iterative schemes for ab initio total-energy calculations using a plane-wave basis set. *Phys. Rev. B* **54**, 11169–11186 (1996).

47. Perdew, J. P., Ernzerhof, M. & Burke, K. Rationale for mixing exact exchange with density functional approximations. *J. Chem. Phys.* **105**, 9982–9985 (1996).
48. Perdew, J. P., Burke, K. & Ernzerhof, M. Generalized gradient approximation made simple. *Phys. Rev. Lett.* **77**, 3865–3868 (1996).
49. Zhou, F., Cococcioni, M., Marianetti, C. A., Morgan, D. & Ceder, G. First-principles prediction of redox potentials in transition-metal compounds with LDA+*U*. *Phys. Rev. B* **70**, 235121 (2004).
50. Farnesi Camellone, M. & Marx, D. On the impact of solvation on a Au/TiO_2 nanocatalyst in contact with water. *J. Phys. Chem. Lett.* **4**, 514–518 (2013).
51. Xiao, R., Li, H. & Chen, L. High-throughput design and optimization of fast lithium ion conductors by the combination of bond-valence method and density functional theory. *Sci. Rep.* **5**, 14227 (2015).
52. Adams, S. & Rao, R. P. High power lithium ion battery materials by computational design. *Phys. Status Solidi A* **208**, 1746–1753 (2011).

Acknowledgements

Y. Lu acknowledges the support of the National Key R&D Program of China (2022YFB3807800), Y. Lu, Y.-S.H. and F.D. acknowledge the support of the National Natural Science Foundation (NSFC) of China (52122214, 52394174 and 52202332) and Y. Lu acknowledges the support of the Youth Innovation Promotion Association of the Chinese Academy of Sciences (2020006). Y.-S.H. acknowledges the support of the Strategic Priority Research Program of the Chinese Academy of Sciences (XDA0400000) and the Jiangsu Provincial Carbon Peak and Neutrality Innovation Program (Industry Tackling on Prospect and Key Technology), China (BE2022002-5). We thank the 1W1B beamline of Beijing Synchrotron Radiation Facility for support.

Author contributions

F.D., Y. Lu and Y.-S.H. conceived the idea and directed the project. F.D. synthesized the high-entropy oxide materials and carried out the electrochemical experiments and materials characterization with X.H., Y.Y., Z. Hu, Y.N., Y. Liu and J.Z. P.J., Z. Han, X.R. and D.S. contributed to the FIB and STEM analyses. H.M. contributed to DFT/BV simulations. F.D. wrote the original draft; Y. Lu, H.M., D.S., L.C. and Y.-S.H. reviewed and edited the manuscript. All the authors discussed the results and commented on the manuscript.

Competing interests

The authors declare no competing interests.

Additional information

Supplementary information The online version contains supplementary material available at https://doi.org/10.1038/s41560-024-01616-5.

Correspondence and requests for materials should be addressed to Yaxiang Lu, Huican Mao, Dong Su or Yong-Sheng Hu.

Peer review information *Nature Energy* thanks Shaohua Guo, Weifeng Wei and the other, anonymous, reviewer(s) for their contribution to the peer review of this work.